Publication Year	2022
Acceptance in OA	2025-03-08T17:58:16Z
Title	The MeerKAT Galaxy Cluster Legacy Survey: I. Survey Overview and Highlights
Authors	Knowles, K., Cotton, W. D., Rudnick, L., Camilo, F., Goedhart, S., Deane, R., RAMATSOKU, MPATI ANALICIA, Bietenholz, M. F., Brüggen, M., Button, C., Chen, H., Chibueze, J. O., Clarke, T. E., DE GASPERIN, Francesco, Ianjamasimanana, R., Józsa, G. I.G., Hilton, M., Kesebonye, K. C., Kolokythas, K., Kraan-Korteweg, R. C., Lawrie, G., Lochner, M., Loubser, S. I., Marchegiani, P., Mhlahlo, N., Moodley, K., Murphy, E., Namumba, B., Oozeer, N., Parekh, V., Pillay, D. S., Passmoor, S. S., Ramaila, A. J.T., Ranchod, S., Retana-Montenegro, E., Sebokolodi, L., Sikhosana, S. P., Smirnov, O., Thorat, K., VENTURI, Tiziana, Abbott, T. D., Adam, R. M., Adams, G., Aldera, M. A., Bauermeister, E. F., Bennett, T. G.H., Bode, W. A., Botha, D. H., Botha, A. G., Brederode, L. R.S., Buchner, S., Burger, J. P., Cheetham, T., De Villiers, D. I.L., Dikgale-Mahlakoana, M. A., Du Toit, L. J., Esterhuyse, S. W.P., Fadana, G., Fanaroff, B. L., Fataar, S., Foley, A. R., Fourie, D. J., Frank, B. S., Gamatham, R. R.G., Gatsi, T. G., Geyer, M., Gouws, M., Gumede, S. C., Heywood, I., Hlakola, M. J., Hokwana, A., Hoosen, S. W., Horn, D. M., Horrell, J. M.G., Hugo, B. V., Isaacson, A. R., Jonas, J. L., Jordaan, J. D.B., Joubert, A. F., Julie, R. P.M., Kapp, F. B., Kasper, V. A., Kenyon, J. S., Kotzé, P. P.A., Kotze, A. G., Kriek, N., Kriel, H., Krishnan, V. K., Kusel, T. W., Legodi, L. S., Lehmensiek, R., Liebenberg, D., Lord, R. T., Lunsky, B. M., Madisa, K., Magnus, L. G., Main, J. P.L., Makhaba, A., Makhathini, S., Malan, J. A.
Publisher's version (DOI)	10.1051/0004-6361/202141488
Handle	http://hdl.handle.net/20.500.12386/36550
Journal	ASTRONOMY & ASTROPHYSICS
Volume	657

Table 4. Catalogue of the 99 diffuse cluster radio sources detected in the MGCLS.

(1) Cluster name	(2) RA_{J2000} (deg)	(3) Dec_{J2000} (deg)	(4) z	(5) Class	(6) New?	(7) LAS (′)	(8) LLS (Mpc)	(9) Notes [Refs.]
Abell 13	3.384	−19.501	0.094	cR		3.0	0.32	W of centre; [8, 13, 17, 37]
Abell 22	5.161	−25.722	0.142	cH		2.7	0.41	[8]
Abell 85	10.453	−9.318	0.056	MH (†)	✓	4.0	0.26	
				Ph [a]		5.6	0.36	SW of centre; [8, 18]
Abell 168	18.791	0.248	0.045	R		12.4	0.66	N of centre; [10]
Abell 209	22.990	−13.576	0.209	H		7.9	1.62	Embedded HT; [17, 19, 20, 41, 42]
Abell 370	39.960	−1.586	0.375	cH	✓	3.1	0.96	[44]
Abell 521	73.536	−10.244	0.248	R		6.0	1.40	SE of centre; [11, 15, 28, 41]
				H		5.3	1.23	[4, 6, 20, 28, 42]
				R	✓	4.0	0.93	NW of centre
Abell 545 [b]	83.102	−11.543	0.154	H		4.7	0.75	[1, 17]
Abell 2645	355.320	−9.028	0.251	cH	✓	2.7	0.64	Irregular shape; [5]
Abell 2667	357.920	−26.084	0.232	H (†)		4.6	1.02	[16]
Abell 2744	3.567	−30.383	0.307	H		7.5	2.04	[8, 13, 17, 21, 32, 42]
				R		5.8	1.57	NE of centre; [8, 13, 21, 30, 32, 42]
				R		4.6	1.25	SE of centre; [32]
Abell 2751	4.058	−31.389	0.081	cPh	✓	0.9	0.08	NW of centre; [8] (says relic)
Abell 2811	10.537	−28.536	0.108	H		5.2	0.62	[8]
Abell 2813	10.852	−20.621	0.292	cH	✓	3.1	0.81	
Abell 2895	19.546	−26.973	0.228	cPh	✓	0.8	0.18	E of centre
Abell 3365	87.050	−21.935	0.093	R	✓	6.8	0.70	NE of centre; [45]
				R	✓	3.4	0.35	W of centre; [45]
Abell 3376	90.426	−39.985	0.047	R		28.1	1.55	E of centre; [2, 12, 23]
				R		18.8	1.04	W of centre; [2, 12, 23]
Abell 3558	201.978	−31.492	0.048	H		4.5	0.25	[7, 39]
Abell 3562	202.783	−31.673	0.050	H		11.5	0.67	[7, 14, 40]
				R		8.6	0.50	SW of centre; [40]
Abell 3667	303.140	−56.841	0.056	R		25.8	1.67	SE of centre; [22, 33]
				R		35.2	2.28	NW of centre; [22, 33]
Abell 4038	356.880	−28.203	0.030	cMH	✓	4.5	0.16	Embedded HT
Abell S295	41.400	−53.038	0.300	H		4.0	1.07	[46]
Abell S1063	342.181	−44.529	0.348	H		5.5	1.62	[44]
Abell S1121	351.284	−41.212	0.190	U		2.2	0.42	SE of centre
Bullet	104.658	−55.950	0.297	H		8.5	2.26	[26, 35]
				R		3.8	1.01	E of centre; [36]
El Gordo	15.719	−49.250	0.870	H		3.3	1.53	[3, 27]
				R		2.0	0.93	NW of centre; [3, 27]
				R		1.0	0.46	SE of centre; [3, 27]
				R		0.9	0.42	E of centre; [27]
PLCK G200.9−28.2	72.587	−2.949	0.220	R	✓	5.6	1.19	E of centre
				R	✓	2.7	0.58	SW of centre; [24]
				cR	✓	1.0	0.21	NW of centre

Notes. Several of the 62 MGCLS clusters in this catalogue are host to more than one diffuse cluster source. Columns: (1) Cluster name; (2) and (3) NED cluster position: J2000 RA and Dec; (4) Cluster redshift; (5) Diffuse source classification – mini-halo (MH), halo (H), relic (R), phoenix (Ph), candidate (c), unknown/unclear (U); see Sect. 6 for further details. Elongated halos/halo candidates with embedded bright AGN sources are indicated by (†); (6) Indicates whether or not the diffuse source is a new detection; (7) Largest angular size in arcminutes; (8) Largest physical linear size at the cluster redshift in Mpc; (9) Notes on the detection with references, in square brackets, to previous studies. HT – head-tail galaxy; WAT – wide-angle tail galaxy. [a]Mixed classification in the literature (see Sect. 6.1.1). [b]Diffuse emission from the Hα region in the Orion Nebula is also detected in this field. [c]MACS J0257.6−2209 has a published detection of a giant radio halo (Giacintucci et al. 2017) but in the higher-quality MGCLS data, the reported giant halo looks like the blending of other sources. [d]Diffuse emission in RXC J0520.7−1328 is complex and difficult to classify (see Sect. 6.1.2).

References. [1] Bacchi et al. (2003); [2] Bagchi et al. (2006); [3] Botteon et al. (2016); [4] Brunetti et al. (2008); [5] Cassano et al. (2013); [6] Dallacasa et al. (2009); [7] Di Gennaro et al. (2018b); [8] Duchesne et al. (2021a); [9] Dwarakanath et al. (2011); [10] Dwarakanath et al. (2018); [11] Ferrari et al. (2006); [12] George et al. (2015); [13] George et al. (2017); [14] Giacintucci et al. (2005); [15] Giacintucci et al. (2008); [16] Giacintucci et al. (2017); [17] Giovannini et al. (1999); [18] Giovannini & Feretti (2000); [19] Giovannini et al. (2006); [20] Giovannini et al. (2009); [21] Govoni et al. (2001); [22] Hindson et al. (2014); [23] Kale et al. (2012); [24] Kale et al. (2017); [25] Kale et al. (2019); [26] Liang et al. (2000); [27] Lindner et al. (2014); [28] Macario et al. (2013); [29] Macario et al. (2014); [30] Orrù et al. (2007); [31] Parekh et al. (2017); [32] Pearce et al. (2017); [33] Rottgering et al. (1997); [34] Sandhu et al. (2018); [35] Shimwell et al. (2014); [36] Shimwell et al. (2015); [37] Slee et al. (2001); [38] Stuardi et al. (2019); [39] Venturi et al. (2000); [40] Venturi et al. (2003); [41] Venturi et al. (2007); [42] Venturi et al. (2013); [43] Wilber et al. (2020); [44] Xie et al. (2020); [45] van Weeren et al. (2011b); [46] Knowles et al. (2021); [47] HyeongHan et al. (2020); [48] Feretti et al. (2005). We note that after our review of the literature, detections of diffuse emission in some of the clusters above are published by Duchesne et al. (2021b), Brüggen et al. (2021) and Duchesne et al. (2021c).

Table 4. continued.

(1) Cluster name	(2) RA_{J2000} (deg)	(3) Dec_{J2000} (deg)	(4) z	(5) Class	(6) New?	(7) LAS (′)	(8) LLS (Mpc)	(9) Notes [Refs.]
MACS J0257.6−2209 [(c)]	44.412	−22.163	0.322	U		1.6	0.45	[16]
				cR	✓	1.4	0.39	SW of centre
MACS J0417.5−1154	64.394	−11.909	0.443	H [(†)]		4.9	1.68	[9, 31, 34]
				cR	✓	1.0	0.34	N of centre
				cR	✓	1.0	0.34	NW of centre
RXC J0510.7−0801	77.685	−8.020	0.220	cH [(†)]	✓	4.9	1.04	
				cR	✓	3.0	0.64	N of centre; possible WAT
RXC J0520.7−1328 [(d)]	80.200	−13.502	0.336	cR		4.2	1.21	SE of centre; [29]
				U		7.1	2.05	SE of centre; bubble?; [29]
RXC J1314.4−2525	198.599	−25.256	0.244	H		4.7	1.08	[38, 48]
				R		4.7	1.08	W of centre; [38, 48]
				R		2.7	0.62	E of centre; [38, 48]
RXC J2351.0−1954	357.770	−19.913	0.248	cR		9.8	2.28	W of centre; [8]
				cR		5.5	1.28	E of centre; [8]
				cH	✓	4.0	0.93	[8]
J0027.3−5015	6.839	−50.251	0.145	cMH	✓	2.5	0.38	
J0145.0−5300	26.260	−53.014	0.117	H	✓	4.9	0.62	
J0145.2−6033	26.320	−60.565	0.181	cMH	✓	1.9	0.35	
J0216.3−4816	34.080	−48.273	0.163	cMH	✓	1.4	0.24	
J0217.2−5244	34.303	−52.747	0.343	cR	✓	1.5	0.44	N of centre
J0225.9−4154	36.478	−41.910	0.220	H	✓	2.4	0.51	
J0232.2−4420	38.070	−44.348	0.284	H		5.8	1.49	[25]
				cR	✓	3.3	0.85	S of centre
				cR	✓	1.8	0.46	E of centre
J0303.7−7752	45.943	−77.869	0.274	H	✓	3.8	0.95	
J0314.3−4525	48.583	−45.424	0.072	cMH	✓	2.4	0.20	
J0342.8−5338	55.725	−53.635	0.060	MH [(†)]	✓	5.2	0.36	
J0351.1−8212	57.787	−82.217	0.061	U	✓			See Sect. 6.2.2
J0352.4−7401	58.123	−74.031	0.127	R	✓	15.6	2.13	SE of centre
				H	✓	10.7	1.46	
				cR	✓	6.8	0.93	NW of centre
				R	✓	3.9	0.53	NNW of centre
				R	✓	5.0	0.68	N of centre
J0431.4−6126	67.850	−61.444	0.059	R	✓	9.7	0.66	SE of centre
				U	✓			Confused tail
J0510.2−4519	77.558	−45.321	0.200	cMH	✓	1.3	0.26	
J0516.6−5430	79.158	−54.514	0.295	H	✓	5.7	1.51	
				R	✓	5.7	1.51	N of centre
				cR	✓	2.3	0.61	S of centre
J0528.9−3927	82.235	−39.463	0.284	H		4.0	1.06	[46]
J0627.2−5428	96.810	−54.470	0.051	R	✓	5.4	0.32	W of centre
J0631.3−5610	97.836	−56.172	0.054	cR	✓	7.7	0.49	W of centre
J0637.3−4828	99.329	−48.478	0.203	U	✓	7.6	1.52	
				cR	✓	2.0	0.40	NW of centre
J0638.7−5358	99.694	−53.972	0.227	H [(†)]		6.4	1.40	[43]
J0645.4−5413	101.372	−54.219	0.164	H	✓	7.7	1.30	
				R	✓	3.5	0.59	SW of centre
J0745.1−5404	116.290	−54.079	0.074	U	✓	4.2	0.35	S of centre
J0820.9−5704	125.248	−57.080	0.061	U	✓			S of centre
J1130.0−4213	172.523	−42.230	0.155	cR	✓	2.1	0.34	NE of centre
J1423.7−5412	215.930	−54.203	0.300	U	✓			N of centre
J1539.5−8335	234.891	−83.592	0.073	MH	✓	2.8	0.23	
				cR	✓	2.2	0.18	W of centre
J1601.7−7544	240.445	−75.746	0.153	H	✓	5.9	0.94	
J1840.6−7709	280.155	−77.156	0.019	cMH	✓	2.5	0.06	
J2023.4−5535	305.852	−55.592	0.232	H		4.7	1.04	[47]
				R		2.9	0.64	[47]

angular size of 5.6′ (∼370 kpc). This structure has not been detected in any of the low resolution radio data available in the literature at other frequencies (see Duchesne et al. 2021a, and references therein), possibly due to its low surface brightness (∼1.1 μJy arcsec^{-2} in the diffuse emission filtered 25″ resolution image) and its proximity to the 27 mJy BCG and 13 mJy tailed source. Given its size and location in a cool-core system, we classify this new detection as a mini-halo. We note, however, that

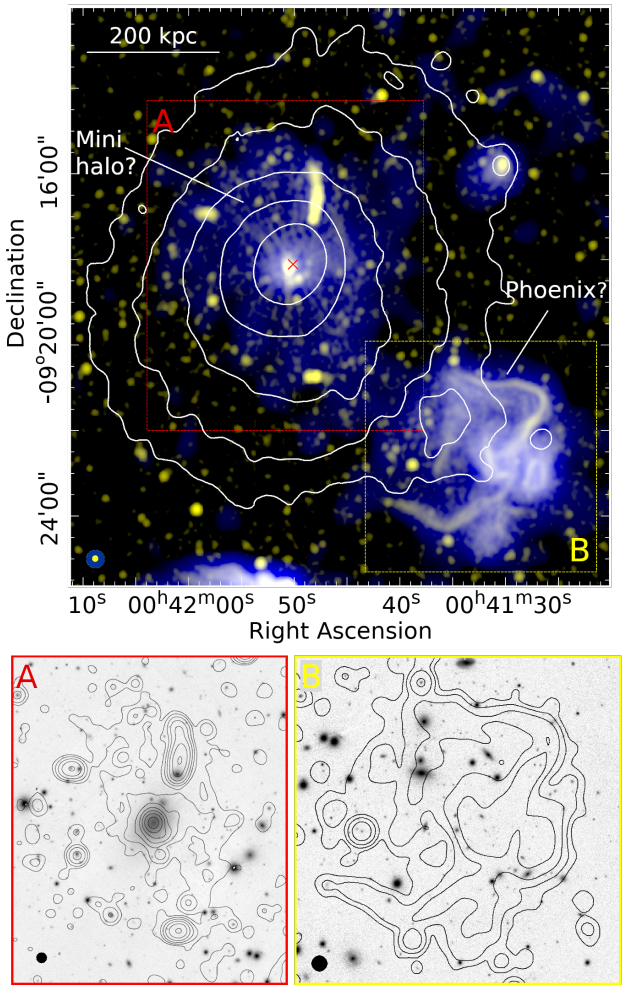

Fig. 8. Multi-resolution MGCLS view of Abell 85. *Top*: full-resolution ($7.7'' \times 7.1''$; yellow, log scale between 0.006 and 2 mJy beam^{-1}) and filtered 25″ resolution (blue, log scale between 0.06 and 3 mJy beam^{-1}) Stokes-*I* intensity image of Abell 85, with the bright BCG and tailed radio galaxy emission filtered out. Smoothed archival *Chandra* 0.5–7 keV X-ray contours (levels: 1.0, 1.7, 3.4, 6.8, 13.6×10^{-7} counts cm^{-2} s^{-1}) are overlaid in white. The respective synthesised MGCLS beams are shown on the lower left. The physical scale at the cluster redshift is indicated on the upper left, and the red × marks the NED cluster position. A newly detected elongated mini-halo (largest linear size ∼370 kpc) is seen around the cluster BCG. Filamentary structures are seen in the known phoenix/revived fossil plasma source SW of the cluster. *Bottom*: Pan-STARRS *r*-band images of the boxed regions from the top panel, with MGCLS 15″ resolution contours overlaid. Contour levels start at $3\sigma = 30$ μJy beam^{-1} and increase by factors of 3.

the MGCLS contains discoveries of several other examples of elongated diffuse halos with embedded central radio-loud BCGs (indicated by (†) in Table 4 at the end of the paper), some of which are on megaparsec scales. We may be observing a new type of diffuse structure, bridging both halo and mini-halo classifications. A handful of cool-core clusters have been found to host larger scale radio halos (Bonafede et al. 2014; Sommer et al. 2017), and in each case the cluster shows signs of merger activity in addition to the cool X-ray core, as is the case for Abell 85 (Yu et al. 2016).

The phoenix source has been studied at multiple frequencies (Slee & Reynolds 1984; Slee et al. 1994, 2001; Giovannini & Feretti 2000; Duchesne et al. 2021a), variously classified as a revived fossil plasma source, a phoenix, and a relic. At full resolution (yellow in Fig. 8), MeerKAT images this source in unprecedented detail, resolving a large number of filamentary structures extending from a brighter complex core region. At the filtered 25″ resolution (blue in Fig. 8) we recover the full angular extent of the source as seen at lower frequencies (Duchesne et al. 2021a). The diffuse emission extends far from the filaments, suggesting that some form of distributed reacceleration is necessary.

The source's complex morphology could result from recurrent episodes of AGN activity, although determining the host galaxy(ies) for these structures is not trivial. Several potential hosts can be seen in the Pan-STARRS *r*-band image in Fig. 8. Sub-arcsecond resolution imaging is needed to identify the radio core(s), if present, in order to cross-match with optical counterpart(s). The toroidal structure in the western region of the source may indicate late stage radio-mode feedback in a non-central cluster galaxy source (such as in M 87, Nakamura & Asada 2013; Walker et al. 2018), possibly caused by an evolved radio lobe that has been transformed into a 'smoke-ring'-like feature (Enßlin & Brüggen 2002). Such vortex structures can travel much further than amorphous plasma structures can, as shown by hydrodynamical simulations (Turner & Taylor 1957), and the radio features here could therefore be at a more advanced stage than the radio emission in M 87. The buoyancy produced by this off-centre bubble is sufficiently powerful to uplift the ICM, visible in the *Chandra* X-ray contours in Fig. 8. Filamentary wings of radio emission trail the bubble for about 200 kpc (at the cluster redshift). The filaments are quite narrow (10–20 kpc), which constrains transport parameters for the enclosed cosmic-ray electrons, as well as ambient turbulent motions that would disrupt such structures (de Gasperin et al. 2017). Such filaments can survive in turbulent motions provided that there are Reynolds stresses of magnetic fields that thread the wings (Banda-Barragán et al. 2018). Determining the Alfvén scale – the physical scale at which the magnetic tension starts to play a role in turbulent dynamics – may assist in clarifying their role.

Spectral information can help constrain the history of the cosmic-ray population in the phoenix source. From the full source volume, we measure a flux density of $S_{1283\,\mathrm{MHz}} = 242.4 \pm 12.1$ mJy. Comparing to a flux density of $S_{148\,\mathrm{MHz}} = 9.82 \pm 0.98$ mJy within the same solid angle from TGSS (Intema et al. 2017), we obtain a steep integrated spectrum of $\alpha_{148}^{1283} = -1.7 \pm 0.3$ for the full source. This latter value is in agreement with the 148–300 MHz spectral index of -1.85 ± 0.03 derived by Duchesne et al. (2021a). The brightest regions of the complex structure have sufficient S/N across the MeerKAT bandwidth to determine in-band spectral indices, and we find values[11] ranging from −2.9 to −3.5. The steep spectra of the diffuse and filamentary structures indicate old electron populations; however, the cause of the extreme steep spectrum in the central regions is unclear. There may be an artificial steepening effect from the frequency-dependent *uv*-coverage; although this should not be important in the brightest fine scale structures, this requires further investigation.

6.1.2. RXC J0520.7−1328: Revealing a diffuse multiplex

The MGCLS reveals complex structures in the previously studied cluster RXC J0520.7−1328 (also known as

[11] Statistical uncertainties on the in-band spectral index are less than 0.05 in these regions.

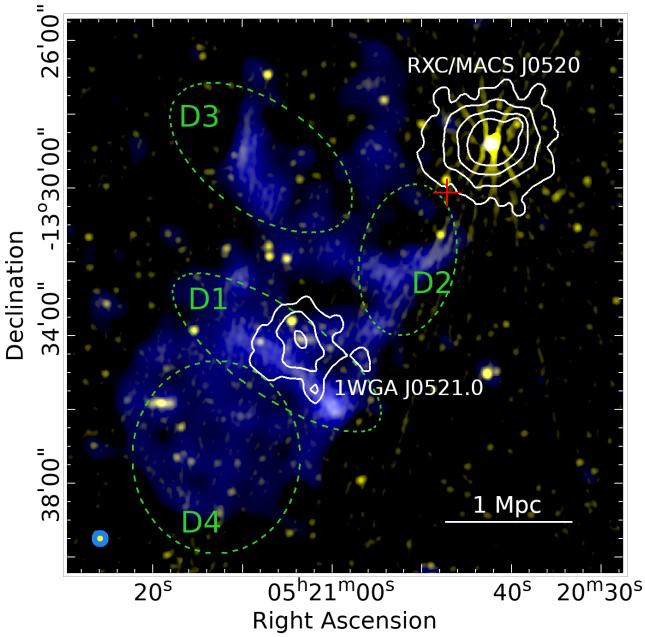

Fig. 9. MGCLS full-resolution (8.6″; yellow) and diffuse emission filtered 25″ resolution (blue) Stokes-*I* intensity image of a portion of the RXC J0520.7−1328 field, showing complex extended emission within the region. The corresponding synthesised beams are shown on the lower left by the filled yellow and blue ellipses, respectively. The colour scales are in square root scaling between 10−500 μJy beam^{-1} (yellow) and 20−500 μJy beam^{-1} (blue). The physical scale at the cluster redshift is indicated on the lower right, and the cross marks the NED cluster position. Smoothed archival *Chandra* 0.5−7 keV X-ray contours (levels: 3, 6, 12, 24×10^{-8} counts cm^{-2} s^{-1}) are overlaid in white, with RXC J0520.7−1328 and its companion cluster 1WGA J0521.0−1333 labelled. Dashed green ellipses indicate the regions of diffuse emission, D1 to D4, identified in Macario et al. (2014). The full-resolution MGCLS image contains artefacts that radiate from the bright compact source in RXC J0520.7−1328.

MACS J0520.7−1328, Ebeling et al. 2001) that do not obviously fit any of the existing paradigms. RXC J0520.7−1328, at $z = 0.336$, is part of a possible cluster pair, with its companion, 1WGA J0521.0−1333, lying to the south-east at a redshift of $z = 0.34$ (Macario et al. 2014). Multi-resolution MGCLS images of this pair, presented in Fig. 9, show a large, complex, diffuse source south-east of RXC J0520.7−1328, coincident in part with 1WGA J0521.0−1333. The brightest portion of the radio emission is a bar-like feature seen at both full (8.6″; yellow) and 25″ (blue) resolution, at the south-east edge of 1WGA J0521.0−1333's X-ray emission. This feature was observed with the GMRT at 323 MHz (Macario et al. 2014), along with three other distinct regions of faint diffuse emission (labels D2 to D4 in Fig. 9, taken from Macario et al. 2014). Although characterised as a relic by Macario et al. (2014), the bar's south-west end is significantly brighter in the full-resolution MeerKAT image than the rest of the feature, and could instead be a head-tail galaxy. Although no MeerKAT polarisation maps are available for this system, spatial spectral index studies may be able to disentangle these two possibilities.

The filtered 25″ resolution MGCLS image shows that the bar-like feature is connected to two other low-surface-brightness structures: a filled circular 'bubble' overlapping the south-east region of 1WGA J0521.0−1333, coincident with the 323 MHz D4 source, and a partial ring or arc of radio emission lying between the two clusters (incorporating sources D2 and D3). MeerKAT reveals much more detail and extent to the complex emission seen at lower frequency. It also reveals a new faint structure (∼0.8 μJy arcsec^{-2} surface brightness) to the east of RXC J0520.7−1328. Despite the improved sensitivity, due to the location and morphology of the structures, it remains difficult to classify the majority of the emission in terms of typical cluster-related nomenclature. A more detailed analysis, including deeper X-ray data, polarimetry, and spectral index studies, will be required to resolve the nature of this emission.

6.1.3. Abell 3667: Polarisation with MGCLS

Radio relics are among the most polarised radio sources known, reaching 70% polarisation levels in localised regions (van Weeren et al. 2010; Loi et al. 2017). Here we showcase the MGCLS dataset's ability to probe polarisation structure in diffuse sources on ∼10″ scales by presenting initial results from polarised observations of the north-west radio relic in the Abell 3667 galaxy cluster ($z = 0.056$). This relic is one of the most impressive examples of radio emission generated by a merger shock wave (Rottgering et al. 1997; Johnston-Hollitt 2003). The shock wave propagates in the ICM with a speed of 1200 km s^{-1}, at roughly two times the sound speed (Finoguenov et al. 2010). The polarisation is maximal close to the shock front, as well as in other regions of the radio relic where the magnetic field is likely compressed and aligned by the action of the shock wave (Ensslin et al. 1998).

In Fig. 10 we see that the magnetic field appears aligned with the NW edge of the radio relic at the location of the shock; this is seen in other radio relics as well (see e.g. van Weeren et al. 2010; Ozawa et al. 2015). We also observe a patchy, disordered structure to the magnetic field away from the edge; this is seen in other relics, and is expected as turbulence develops post-shock (Kang 2017). In Abell 3667, we can rule out disorder due to Faraday rotation in the ICM since we removed these effects using the RMs shown in panel C of Fig. 1. At the same time, the RM is seen to increase from the north towards the central regions of the relic; this could be due to the sub-cluster identified in that region with X-ray observations (Finoguenov et al. 2010), if it is located in front of the radio emitting plasma.

6.2. New clusters with diffuse emission

There are 34 MGCLS clusters in which we detect cluster diffuse emission for the first time. Here we present three examples that raise interesting science issues and showcase the capabilities of the MGCLS.

6.2.1. J0352.4−7401: Multiple relics in a massive merger

The MGCLS has detected several new relics, many with large-scale filamentary structure. One such example is the newly detected SE relic in MCXC J0352.4−7401 (Abell 3186, $z = 0.1270$) shown in Fig. 11. The relic, located approximately 1.2 Mpc SE of the cluster centre, is very large, 2 Mpc long and 340 kpc wide. The brightest region of the SE relic is a straight bar, aligned N–S and spatially connected to a 3 mJy compact source (marked by the black cross). No optical counterpart is visible in the Digitized Sky Survey (DSS). The in-band spectral index map of the SE relic, also in Fig. 11, shows this compact source to have a significantly flatter spectrum ($\alpha \sim -0.4$) than that of the bar ($\alpha \sim -1.0$ to -1.2). The overall shape of the relic is curved, with the southern part consisting of two parallel

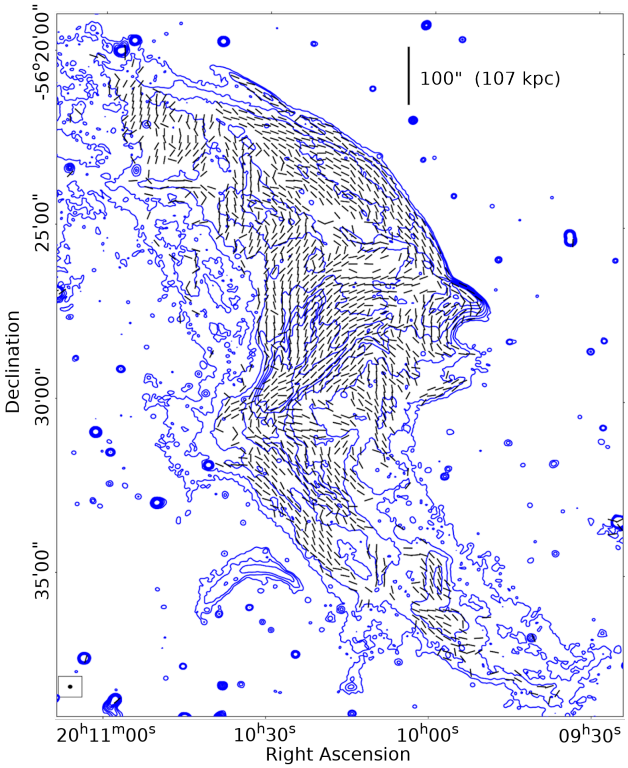

Fig. 10. Inferred magnetic field angles for the north-west relic in Abell 3667, after correction for Faraday rotation (which is shown in Fig. 1). Blue contours show the full-resolution (7.5″ × 7.4″) Stokes-*I* MGCLS intensity, with the synthesised beam shown in the boxed region on the lower left. Contour levels are 10, 20, 40, 60, 80, 100 × 1σ, where σ = 6.7 μJy beam^{-1}. Magnetic field vectors (angles only) are shown where the linearly polarised intensity is >8σ. The magnetic field is highly ordered along the NW edge of the relic.

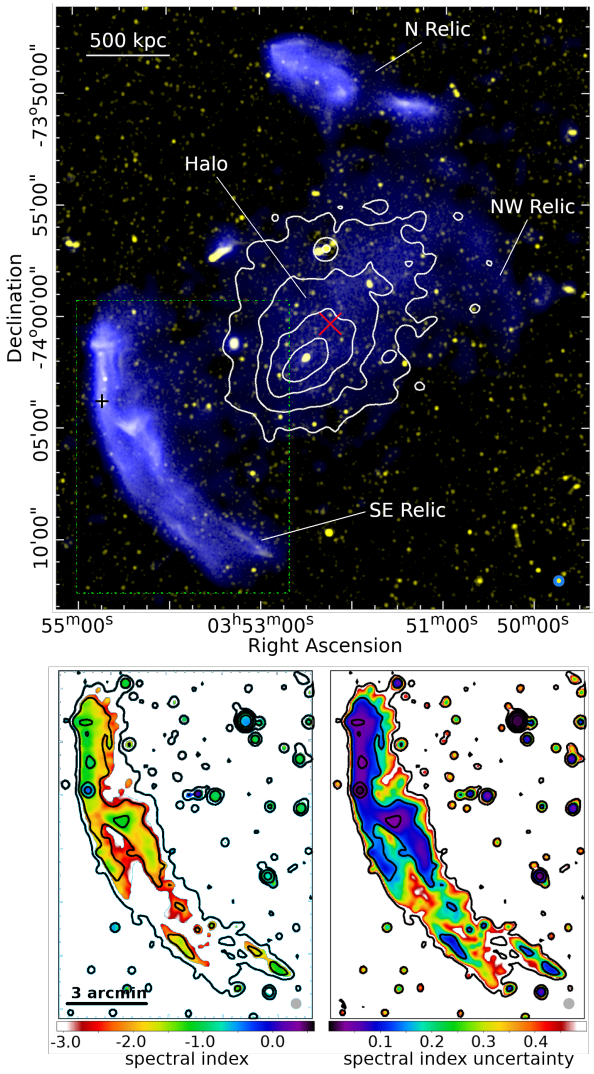

Fig. 11. MGCLS view of the newly detected multiple-relic and radio halo system in MCXC J0352.4−7401. *Top*: MGCLS full-resolution (7.0″ × 6.8″; yellow) and filtered 25″ resolution (blue) Stokes-*I* intensity images. The colour scales are in square root scaling between 50–500 μJy beam^{-1} (yellow) and 5–300 μJy beam^{-1} (blue). Synthesised MGCLS beams are shown on the lower right, and the physical scale at the cluster redshift is shown on the upper left. The red × marks the NED cluster position, and the black cross indicates the position of a 3 mJy compact source coincident with the SE relic. Smoothed archival *Chandra* 0.5–7 keV contours (levels: 4, 8, 16, 30 × 10^{-7} counts cm^{-2} s^{-1}) are overlaid in white. *Bottom*: in-band spectral index (*left*) and spectral index uncertainty (*right*) maps of the dashed region from the top panel, with 15″ resolution MGCLS intensity contours overlaid. Contours start at 5σ = 40 μJy beam^{-1} and increase in factors of 4. The synthesised beam is indicated by the filled grey circle on the lower right of each panel.

filaments with complex structure. The filaments have steeper spectra than the northern bar, with in-band spectral indices of −1.5 at the centre of the filaments, steepening to −2.5 at the edges. The trailing edge of the relic is much wider in 25″ resolution imaging of the field (shown in blue in the top panel of Fig. 11), with a maximum width of ∼580 kpc. The SE relic has a measured 1.28 GHz flux density of ∼65 mJy, which corresponds to a total radio power of $P_{1.28\,\mathrm{GHz}} \sim 2.8 \times 10^{24}$ W Hz^{-1}.

This system also hosts a smaller 1.1 Mpc relic north of the cluster, as well as a large radio halo that fills the X-ray emitting region. The N relic has two components in the full-resolution image and its morphology is strikingly linear, reminiscent of revived radio galaxies, although no obvious optical counterpart is seen in DSS images. Both the SE and N relics lie far beyond the observed thermal ICM (shown by white *Chandra* contours in Fig. 11). The large-scale radio halo, with a 1.28 GHz flux density of ∼20 mJy, lies at the centre of the cluster, and its SE–NW elongated morphology closely follows that of the X-ray emission. This giant radio halo, with a largest linear size of 1.5 Mpc, has a faint (∼0.2 μJy arcsec^{-2}) diffuse arc-like protrusion off its NW edge, mirroring the SE relic. As the shape and position of the arc-like structure may hint at the presence of another shock front, we classify it as a candidate relic.

The presence of the multiple relics, and their location with respect to the asymmetric X-ray emission, are indicative of a major cluster merger. Recent numerical simulations of galaxy cluster mergers suggest that a merger shock may gradually detach from the dense merging clumps (Zhang et al. 2020), and propagate to the cluster outskirts. There is observational radio evidence for the presence of such merger shocks in the periphery of clusters, for example in the Coma cluster (Giovannini et al. 1991; Brown & Rudnick 2011) and in Abell 2744 (Pearce et al. 2017; Venturi et al. 2013). Given that the N and SE relics lie far beyond the detectable X-ray emitting region, MCXC J0352.4−7401 may be in an advanced merger state, with the merger-induced shocks having propagated into the